Investigation of the Vertical Structure of Warm-Cloud Microphysical Properties Using the Cloud Evolution Diagram, CFODD, Simulated by a Three-Dimensional Spectral Bin Microphysical Model

YOUSUKE SATO

Atmosphere and Ocean Research Institute, University of Tokyo, Kashiwa, Chiba, and Japan Society for the Promotion of Science, Chiyoda-ku, Tokyo, Japan

TAKASHI Y. NAKAJIMA

Research and Information Center, Tokai University, Yoyogi, Tokyo, Japan

TERUYUKI NAKAJIMA

Atmosphere and Ocean Research Institute, University of Tokyo, Kashiwa, Chiba, Japan

(Manuscript received 18 September 2011, in final form 11 January 2012)

ABSTRACT

This paper investigates the vertical structure of warm-cloud microphysical properties using a three-dimensional (3D) spectral bin microphysical model. A time series of contoured frequency by optical depth diagrams (CFODDs), which were proposed by previous studies, are calculated for the first time by a 3D model assuming two types of aerosol conditions (i.e., polluted and pristine). This contrasts with previous studies that obtained CFODDs using either a two-dimensional model or an accumulation of monthly and global observation data. The results show that the simulated CFODDs are characterized by distinctive patterns of radar reflectivities, similar to the patterns often observed by satellite remote sensing, even though the calculation domain of this study is limited to an area of 30×30 km^2, whereas the satellite observations are of a global scale. A cloud microphysical box model is then applied to the simulated cloud field at each time step to identify the dominant process for each of the patterns. The results reveal that the wide variety of satellite-observed CFODD patterns can be attributed to different microphysical processes occurring in multiple cloud cells at various stages of the cloud life cycle.

1. Introduction

Clouds have a large effect on the climate system through the hydrologic cycle and energy budget of the earth. Among the many different types of clouds, low warm clouds critically affect the earth's climate system (Randall et al. 1984; Ma et al. 1996) through their high albedo for solar radiation, which effectively decreases the net radiation at the top of the atmosphere, thus working as an efficient cooler in the climate system. This radiative effect of warm clouds is recognized to be very large; for example, the shortwave forcing by North Pacific stratus region (40°–50°N, 170°W–180°) during June–August (JJA) obtained from 2 yr of Earth Radiation Budget Experiment (ERBE; Barkstorm 1984; Barkstorm and Smith 1986) data can reach approximately -150 W m^{-2} (Klein and Hartmann 1993).

The cloud albedo is mainly determined by the cloud optical thickness (COT), which is a key parameter governing the cloud albedo of solar radiation, and the effective radius (RE), which determines the cloud reflectivity in the shortwave infrared spectral windows. These two parameters are closely related to the microphysical properties of the cloud, such as the liquid water path and the particle size distribution function (SDF). The cloud microphysical properties are affected by cloud–aerosol interactions (Twomey 1974; Albrecht 1989), which cause various complex feedback processes in the earth's energy budget and climate system. The cloud–aerosol interaction

Corresponding author address: Yousuke Sato, Advanced Institute for Computational Science, RIKEN, Kobe, Hyogo 6500047, Japan.
E-mail: yousuke.sato@riken.jp

DOI: 10.1175/JAS-D-11-0244.1

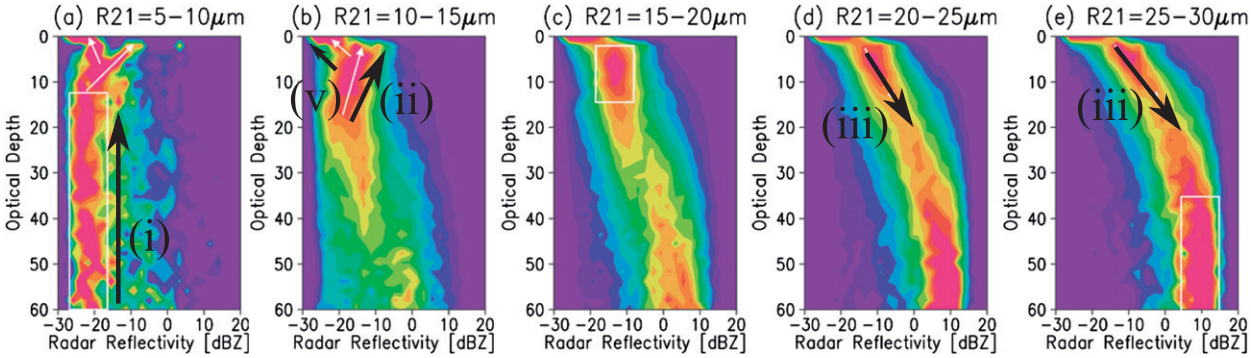

FIG. 1. CFODDs for $r_{2.1}$ = (a) 5–10, (b) 10–15, (c) 15–20, (d) 20–25, and (e) 25–30 μm for the ocean area from June to August 2007. Cited from S10 and rearranged.

is, therefore, one of the key phenomena to be observed and investigated in order to reduce uncertainties in climate prediction.

This background has stimulated a large number of studies to obtain the microphysical and radiative properties of clouds and aerosols from satellites (e.g., Han et al. 1994; Nakajima and Nakajima 1995; Kawamoto et al. 2001; Rosenfeld 2000; Platnick et al. 2003) and aircraft observations (e.g., Nakajima and King 1990; Nakajima et al. 1991; Brenguier et al. 2000; vanZanten and Stevens 2005). Han et al. (1994) and Kawamoto et al. (2001) observed global distributions of COT and RE from Advanced Very High Resolution Radiometer (AVHRR) satellites, and Nakajima and Nakajima (1995) observed these parameters in the region of the 1987 campaign of the First International Satellite Cloud Climatology Project (ISCCP) Regional Experiment (FIRE) (Albrecht et al. 1988). Despite their great contributions to our knowledge, these satellite investigations could only observe the horizontal structure of the cloud properties because of instrument limitations, while the aircraft observations, although able to view the 3D structure of clouds, were limited to narrow spatial regions. Recently, the vertical structure of warm clouds has begun to be observed globally by satellite-borne active sensors [i.e., the *CloudSat* Cloud Profiling Radar (CPR) (Stephens et al. 2008) and *Cloud-Aerosol Lidar and Infrared Pathfinder Satellite* (*CALIPSO*) (Winker et al. 2003, 2007)]. They are in the A-Train satellite constellation (Stephens et al. 2002), which also includes the Moderate Resolution Imaging Spectroradiometer (MODIS) on board the *Aqua* satellite. Nakajima et al. (2010b, hereafter N10) investigated the vertical structure of warm clouds from global-scale observations by the *CloudSat* CPR and *Aqua* MODIS satellite sensors and proposed a new type of diagram, called a contoured frequency by optical depth diagram (CFODD), to interpret the growth process of cloud particles. Suzuki et al. (2010, hereafter S10) also studied CFODDs (Fig. 1) using global *CloudSat* and MODIS data as well as an adiabatic model (Brenguier et al. 2000). They found a multimodal distribution in satellite-observed CFODDs and interpreted these modes as corresponding to evaporation at the cloud top, condensation growth, and the collision process (conversion from cloud particle to rain drop). Their interpretation supported that of N10 regarding the cloud growth regime.

These previous studies formed a basis for the interpretation of various patterns seen in the CFODDs. It should be noted, however, that these analyses only used monthly accumulations of cloud radar and imager data, so we still need to investigate the growth process of cloud particles for each stage of the cloud evolution using a more realistic multiple cloud cell simulation by a three-dimensional (3D) model. In this regard, the most important quantity in the simulation of CFODD is the SDF of the cloud particle polydispersion, and therefore the spectral bin microphysical model (SBM) (e.g., Khain et al. 2000) is an especially useful tool among many types of numerical models to calculate the cloud growth process. Despite the usefulness of the SBM, however, its computational cost is large, and there are few previous studies that examine CFODDs using the model. To our knowledge, there are no studies focusing on the time series of cloud evolution. The objectives of this study are, therefore, to simulate CFODDs by a 3D numerical simulation focusing on the time evolution of clouds and to examine the validity of the interpretations made by N10 and S10.

2. Model description and experimental setup

a. Model description

A 3D SBM called the University of Tokyo Aerosol Cloud Spectral Bin Model (UT-ACBM) (Iguchi et al. 2008; Sato et al. 2009) is used for this study. The dynamical

core of this model is a 3D nonhydrostatic dynamical model (NHM) based on a weather forecasting model developed by the Japan Meteorological Agency (JMA) (Saito et al. 2006; i.e., JMANHM). The turbulence scheme of the NHM is based on that of Deardorff (1980), and the cloud microphysical module is based on the Hebrew University Cloud Model (HUCM; Khain et al. 2000). This model calculates the SDFs of liquid water and six ice hydrometeors [i.e., three ice crystals (plate, column, and dendrite), snowflakes, graupel, and hail]. The SDFs of these seven hydrometeors are represented on each spatial grid by 33 geometrically increasing mass bins that cover particle sizes (melted radii) ranging from 2.0 to 3251 μm. In addition, SDF of aerosol particles is also represented on each spatial grid by 17 geometrically increasing mass bins. Only the warm phase processes of cloud growth (i.e., nucleation, condensation, evaporation, regeneration of aerosols by evaporation, and collision/coagulation) are calculated because the cloud top temperatures of the cloud ensembles targeted in this study are much higher than 273 K in this study.

All aerosols larger than a critical radius are transferred from the aerosol bins to the smallest bin of cloud particles (Suzuki et al. 2006); the critical radius r_{crit} of the aerosols is calculated by the Köhler theory as

$$r_{\mathrm{crit}} = \sqrt{\frac{4}{27}\frac{A^3}{B}\frac{1}{S_w}},$$
$$A \approx \frac{3.3\times 10^{-5}}{T}\,(\mathrm{cm}), \quad B \approx \frac{4.3\nu}{M_{\mathrm{ccn}}}\left(\frac{4\pi\rho_{\mathrm{ccn}}}{3}\right)(\mathrm{cm}), \quad (1)$$

where T, ρ_{ccn}, M_{ccn}, ν, and S_w are the temperature, density of an aerosol particle, molecular weight of the aerosol, Van't Hoff factor (e.g., Low 1969), and supersaturation over water, respectively. Condensation/evaporation growth is calculated by solving an equation (e.g., Rogers and Yau 1989) as

$$\frac{dm}{dt} = \frac{4\pi r S_w}{F}, \quad F = \frac{R_v T}{e_w D_v} + \frac{L_w}{K_a T}\left(\frac{L_w}{R_v T} - 1\right), \quad (2)$$

where m, r, R_v, D_v, e_w, K_a, and L_w are the mass and radius of the hydrometeors, the gas constant of vapor, diffusivity of water vapor, saturation vapor pressure over water, thermal conductivity of air, and specific latent heat of vaporization, respectively. Collision and coagulation growth is calculated using the stochastic collision equation (SCE) (e.g., Pruppacher and Klett 1997)

$$\frac{\partial f(m)}{\partial t} = \int_0^\infty f(m)K(m,m')f(m')\,dm' - \int_0^{m/2} f(m-m'')K(m,m'')f(m'')\,dm'',$$
$$K(m,m') = \pi[r(m)+r'(m')]|V(m)-V(m')|E_{\mathrm{col}}(m,m')E_{\mathrm{coal}}(m,m'), \quad (3)$$

where f, V, E_{col}, and E_{coal} are the SDF of hydrometeors, terminal velocity, collision efficiency, and coalescence efficiency, respectively. A scheme based on a Monte Carlo integration (Sato et al. 2009) is used to calculate Eq. (3) to reduce the computational cost.

Regeneration of aerosols by complete evaporation of cloud water is calculated using the parameterization of Feingold et al. (1996) with the size distribution of the aerosol as

$$R_k(t) = N(t)\frac{\phi_k(t)}{\sum_{k=1}^{n_a}\phi_k(t)}, \quad \phi_k(t) = \frac{\overline{N}_k(0) - \overline{N}_k(t)}{\overline{N}_k(0)}, \quad (4)$$

where $\overline{N}(t)$, $N(t)$, n_a, and $R_k(t)$ are the domain-averaged number of aerosols at time t, the total number of regenerated aerosols, the number of aerosol bins, and the regenerated aerosol number concentration of the kth aerosol bin at time t.

The aerosol number concentration for the initial and boundary conditions of UT-ACBM (Iguchi et al. 2008; Choi et al. 2010) is given by a global aerosol field calculated by Spectral Radiation Transport Model for Aerosol Species (SPRINTARS) (Takemura et al. 2005), an aerosol transport and radiation model coupled with the Model for Interdisciplinary Research on Climate (MIROC) GCM. The "MSTRN-X" radiation code (Sekiguchi and Nakajima 2008; Nakajima et al. 2000) is implemented into UT-ACBM. However, to simplify the experimental setup, which will be described in the next section, a simple radiation parameterization and aerosol distribution are used in this study, instead of the radiation and aerosol schemes of UT-ACBM.

b. Experimental setup

The experimental setup of this study is based on the Dynamics and Chemistry of Marine Stratocumulus Phase II: Entrainment Studies (DYCOMS-II) second research flight (RF02) modeling study (Ackermann et al. 2009), which targeted stratocumulus in the summer season off

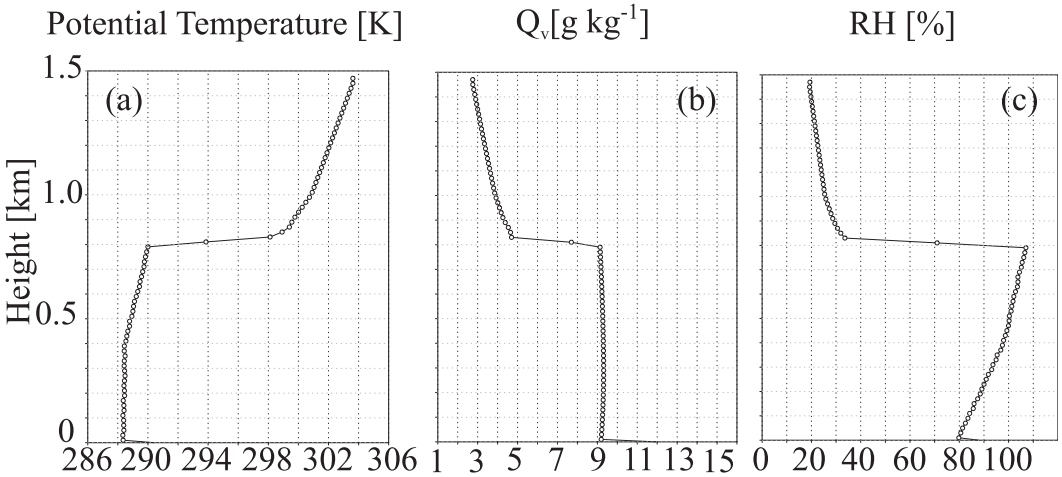

FIG. 2. Initial profiles of (a) potential temperature, (b) vapor mixing ratio, and (c) relative humidity of water.

the coast of California, and whose experimental setup was created from aircraft observations in the region. The initial condition is assumed to be horizontally uniform and without wind. Vertical profiles of the potential temperature, relative humidity, and vapor mixing ratio are shown in Fig. 2. Calculations are started without cloud liquid water, but with a highly saturated layer from 400 to 795 m, which corresponds to the simulated cloud layer. We assume a horizontally and vertically uniform aerosol layer with a lognormal size distribution, whose geometrical standard deviation and mode radius are assumed to be 1.5 and 0.1 μm, respectively. The number concentration of the aerosol is set as 60 cm^{-3} in pristine conditions and 500 cm^{-3} in polluted conditions for sensitivity experiments. The chemical component of the aerosol is sulfate. Calculations are performed for 6 h with a time step of $dt = 0.5$ s on horizontal (vertical) grids with a spacing of 50 (20) m (i.e., $600 \times 600 \times 75$ grids in a domain of $30 \times 30 \times 1.5$ km^3 with a horizontally periodic lateral boundary condition). To drive and maintain warm clouds in the domain, a random perturbation of the potential temperature and vapor mixing ratio is applied, and forcing of the radiation, large-scale subsidence, and surface heat flux is also incorporated, based on the forcing used in Ackermann et al. (2009). Random perturbations of 0.1 K and 0.025 g kg^{-1} are given in the layer below the cloud-top height $z_i = 795$ m at $t = 0$. The large-scale vertical wind is computed as $w_{\mathrm{LS}} = -Dz$, with $D = 3.75 \times 10^{-6}$ s^{-1}, and is used as a source term for each prognostic variable ϕ as $-w_{\mathrm{LS}}\partial\phi/\partial z$. The radiative heating rate is computed at every time step from the divergence of a longwave radiative flux profile in each model column using the parameterization of Stevens et al. (2005):

$$\begin{aligned} F(z) &= F_0 \exp[-Q(z, z_{\mathrm{model\_top}})] + F_1 \exp[-Q(0, z)] \\ &\quad + a\rho_i c_p D H(z - z_i)[0.25(z - z_i)^{4/3} \\ &\quad + zi(z - z_i)^{1/3}] \\ Q(z_1, z_2) &= \int_{z_1}^{z_2} \kappa \rho q_l \, dz. \end{aligned} \tag{5}$$

In Eq. (5), $F_0 = 70$ W m^{-2} and $F_1 = 22$ W m^{-2}, $\rho_i = 1.12$ kg m^{-3}, $c_p = 1004$ J kg^{-1} K^{-1}, H is the Heaviside step function, z_i and $z_{\mathrm{model\_top}}$ are the cloud-top heights and model top heights, $\kappa = 85$ m^2 kg^{-1}, $a = 1$ K m$^{-1/3}$, and q_l and ρ are the liquid water mixing ratio and air density, respectively. The upward sensible and latent heat fluxes from the surface are given as 93 and 16 W m^{-2}, respectively, at each time step. The upward surface momentum flux is computed as $-u_i u_*^2/|U|$, where the wind components u_i and magnitude $|U|$ are defined locally, and the friction velocity is fixed at $u_* = 0.25$ m s^{-2}. To avoid errors caused by model spinup, only the simulated results from 2.5 to 6 h are used to calculate the CFODDs.

The model simulates clouds whose geometrical depth is about 400–500 m in a narrow (30×30 km^2) domain by this experimental setup shown above. The CFODDs in the previous studies were constructed from global observations of warm clouds. Additional global-scale experiments must be performed in the future to extend our understanding of cloud evolution on a global scale.

c. *Calculation of a contoured frequency by optical depth diagram*

To construct a CFODD requires the cloud optical depth (COD) at each model height and the REs

corresponding to those derived from the MODIS satellite. The COD, as denoted by $\tau(z)$ or $\tau_d(z)$, is calculated as

$$\tau_d(z) = \tau(z) = \frac{3}{2\rho_w}\int_{z_{\rm top}}^{z} \frac{q_c(z)}{r_{\rm eff}(z)}\,dz, \tag{6}$$

where ρ_w, $r_{\rm eff}$, $z_{\rm top}$, and z are the density of water, RE, cloud-top height, and height, respectively. Also, q_c is the liquid water content, defined as

$$q_c(z) = \int_{r_{\rm min}}^{r_{\rm max}} \frac{4}{3}\pi\rho_w r^3 f(r,z)\,dr, \tag{7}$$

where f, r, $r_{\rm max}$, and $r_{\rm min}$ are the SDF of cloud particle polydispersion, radius of a cloud particle, and the maximum and minimum radii of cloud particles in the model. RE is defined as

$$r_{\rm eff}(z) = \frac{\int_{r_{\rm min}}^{r_{\rm max}} r^3 f(r,z)\,dr}{\int_{r_{\rm min}}^{r_{\rm max}} r^2 f(r,z)\,dr}. \tag{8}$$

The COT, denoted by τ_c, is then calculated as

$$\tau_c = \frac{3}{2\rho_w}\int_{z_{\rm top}}^{z_{\rm bottom}} \frac{q_c(z)}{r_{\rm eff}(z)}\,dz, \tag{9}$$

where $z_{\rm bottom}$ is the cloud-bottom height.

N10 used RE observed by the 2.1-μm ($r_{2.1}$) or 3.7-μm ($r_{3.7}$) channels of MODIS, and they showed that the 2.1-μm (3.7 μm) channel-observed RE corresponds to the value at a height where the optical depth reaches 15 (8) from the cloud top. In this study, we use the 2.1-μm channel-observed RE, denoted $r_{2.1}$, for calculation of the CFODD. Note that $r_{2.1}$ can be calculated from the following equation (Platnick 2000; Nakajima et al. 2010a):

$$r_{2.1} = \int_0^{\tau_t} r_{\rm eff}[\tau'(z)] w_\lambda(\tau', \tau_t)\,d\tau', \tag{10}$$

where $\tau_t = 8$, the value assumed by Nakajima et al. (2010a), and w_λ is the weight function suggested by Platnick (2000).

To calculate the radar reflectivity for the CFODD, a radar simulator developed by Okamoto et al. (2003, 2007, 2008) is applied to the model outputs. The radar reflectivity of 95 GHz corresponding to the CPR signal Z_e is given as

$$Z_e = Z_{e,\rm true}(z_i)\exp[-2\tau_{d,i-1/2}(z_{i-1/2})] \times \exp\left\{\frac{\exp[-2\sigma_{{\rm ext},ra}(z_i)\Delta z] - 1}{-2\sigma_{{\rm ext},ra}(z_i)\Delta z}\right\}$$

$$Z_{e,\rm true}(z_i) = \frac{\lambda^4}{\pi^5|K|^2}\left[\int_{r_{\rm min}}^{r_{\rm max}} \frac{df(r)}{dr} C_{\rm bk}(r, z_i)\,dr\right], \tag{11}$$

where λ, $C_{\rm bk}(r, z_i)$, $\sigma_{{\rm ext},ra}$, and i are the wavelength of CPR (λ = 3.2 mm, 95 GHz), backscattering cross section, extinction coefficient, and model layer number, respectively. The variables z_i and $\tau_{d,i}$ denote the altitude and optical depth of the center of the ith layer, respectively, and $z_{i-1/2}$ and $\tau_{d,i-1/2}$ denote the altitude and optical depth of the bottom boundary of the ith layer, respectively. Also, K is estimated from the complex refractive index of water m by $|K| = |(m^2 - 1)/(m^2 + 2)|$, and $Z_{e,\rm true}$ is defined as the "true" radar reflectivity (and has dimensions of mm^6 m^{-3}). The exponential terms of Eq. (11) are introduced in order to consider the effects of attenuation at the radar wavelength at each model layer. In this study, the logarithmic form of Z_e is used to describe the radar reflectivity dBZ_e = 10 $\log_{10}(Z_e)$.

Vertical grid resolution for radiative transfer calculation is 10 m (i.e., dz = 10 m), and the profile is made from interpolating results of model results, whose vertical grid spacing is 20 m (i.e., dz = 20 m).

d. Satellite-derived CFODDs

To investigate the regional differences between satellite-derived CFODDs and compare them with model-derived ones, CFODDs are also constructed from satellite observations. CFODDs obtained from satellite observations of a California region (20°–40°N, 115°–135°W) and an East Asian region (20°–40°N, 120°–140°E) are constructed in this study. The former is one of the pristine regions of the globe, and the latter is one of the polluted regions (Nakajima et al. 2001). The radar reflectivity profiles are obtained from the 2B-Geometrical Profiling Product (GEOPROF) of the CloudSat Project (e.g., Mace et al. 2007) for JJA 2007. The COT and RE are obtained from a CPR-matched MODIS multispectral analysis using 2.1-μm radiances (Nakajima et al. 2010a), based on the Comprehensive Analysis Program for Cloud Optical Measurements (CAPCOM; Nakajima and Nakajima, 1995; Kawamoto et al. 2001) algorithm. The COD is obtained by the method of S10, which uses COT and the geometrical depth H_c of the cloud obtained from CPR radar reflectivity. Cloud-top and -bottom heights are determined by the highest and lowest radar bins where the radar reflectivity is larger than the minimum sensitivity of *CloudSat* (−30 dBZ_e).

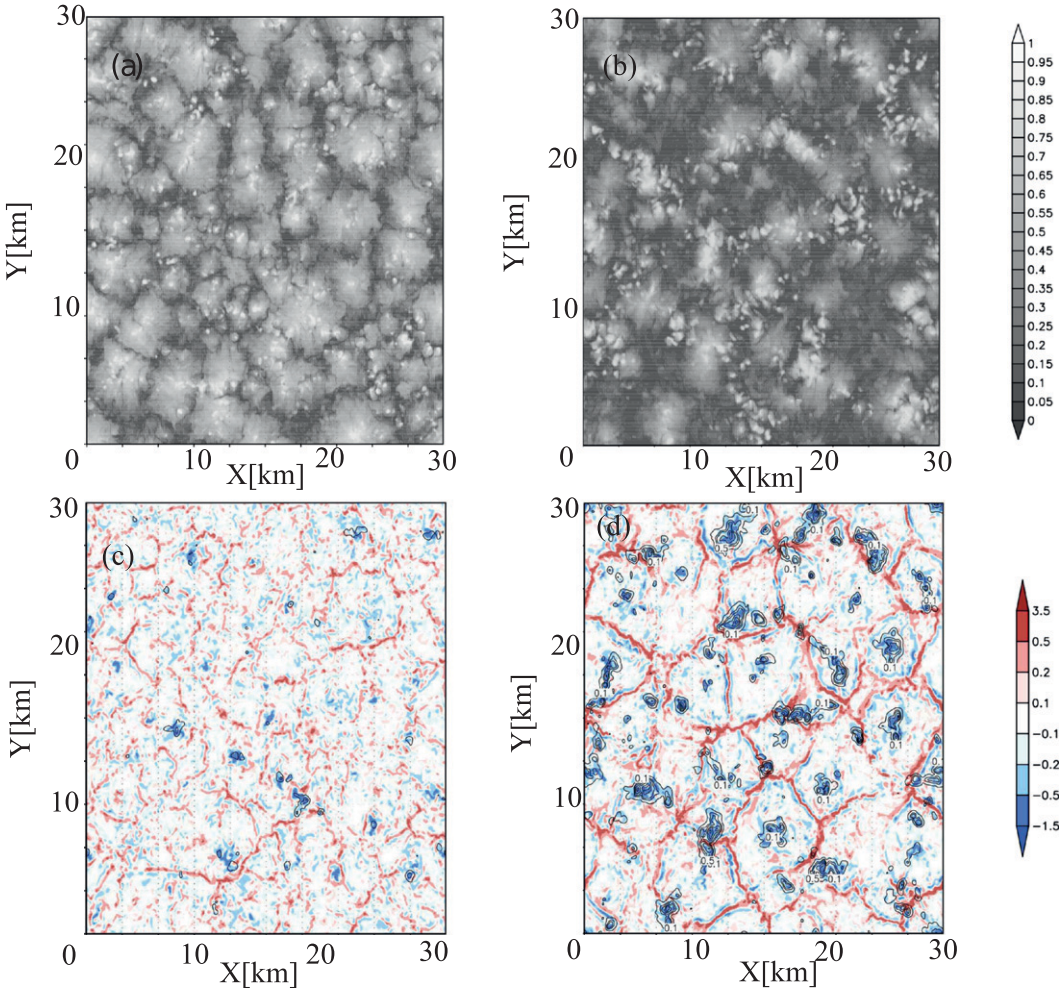

FIG. 3. Areal distributions of the cloud albedo obtained in (a) polluted and (b) pristine experiments, and areal distributions of the vertical wind velocity below the cloud layer (200 m; shading) and surface precipitation (contours) obtained in (c) polluted and (d) pristine experiments. Contours are 0.1, 0.5, 1.0, 2.5, 5.0, and 10.0 mm day^{-1}.

The COD at a height h, measured from the cloud bottom, is calculated by COT and H as

$$\tau(h) = \tau_c\left[1 - \left(\frac{h}{H_c}\right)^{5/3}\right]. \tag{12}$$

The derivation of Eq. (12) is given in S10.

To construct CFODDs for the same conditions as in S10, the procedures shown below are applied to the satellite data. As the sensor on the MODIS satellite is not so sensitive to optically thin cloud, only reflectivity profiles associated with COTs larger than 1 are used for constructing CFODDs. To restrict analyses to warm cloud cases, we use only reflectivity profiles whose cloud-top temperature is estimated to be higher than 273.15 K by both MODIS and the European Centre for Medium-Range Weather Forecasts (ECMWF)-AUX temperature at the CPR echo top. In addition, only single-layer cloud reflectivities are used for the analysis

3. Results

a. *General features of simulated cloud properties and CFODDs*

Figure 3 shows the cloud albedo A field approximated by the formula of Savic-Jovcic and Stevens (2008):

$$A = \tau_c/(6.8 + \tau_c). \tag{13}$$

The figure also presents the vertical wind velocity field below the cloud layer (i.e., 200-m height from the surface) and the simulated surface precipitation rate at 6 h after the start of the calculation. High (low) albedo values are simulated in the polluted (pristine) experiment. It is

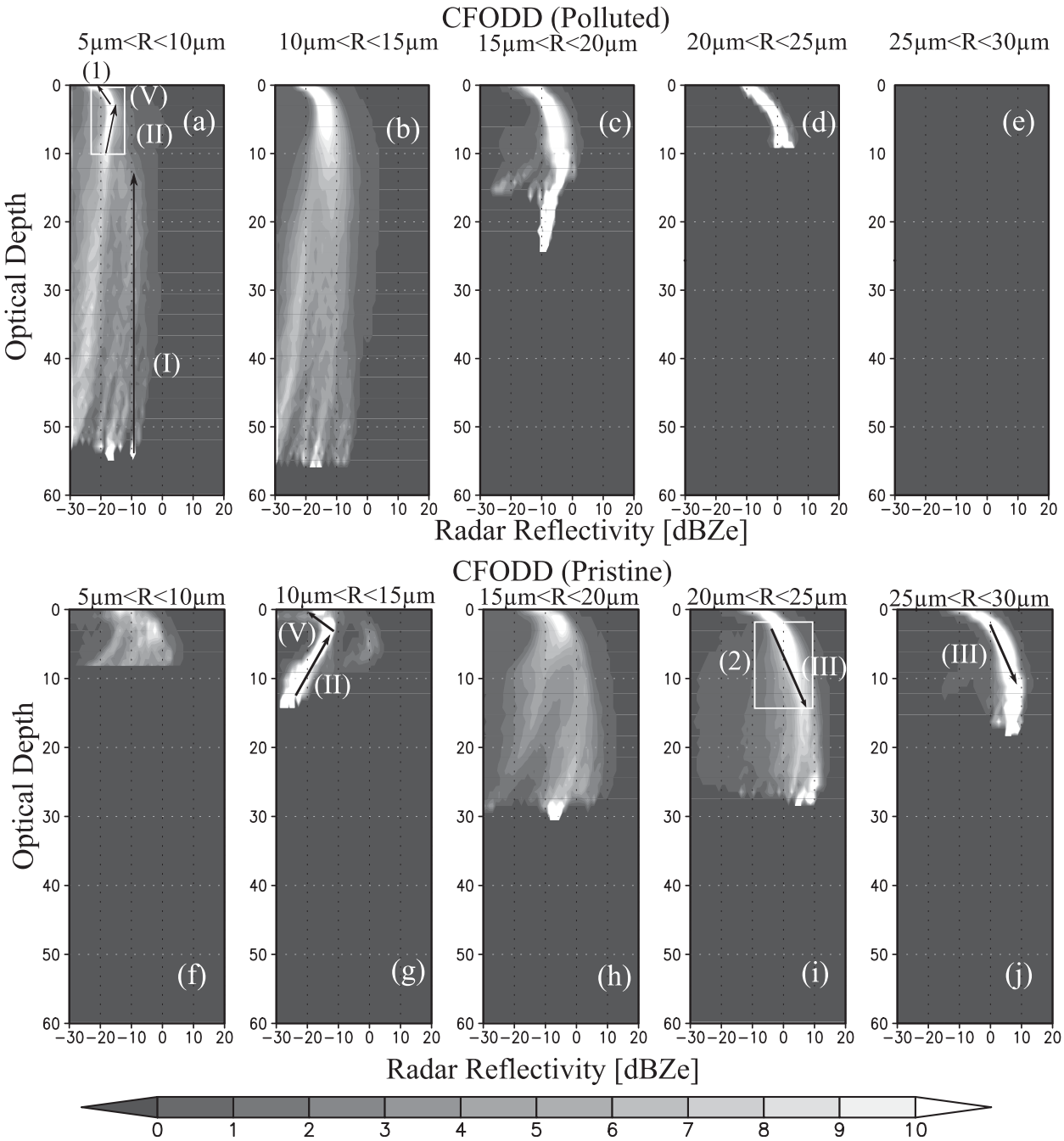

FIG. 4. CFODDs at $t = 6$ h obtained from (a)–(e) polluted and (f)–(j) pristine experiments, divided by RE = (a),(f) 5–10, (b),(g) 10–15, (c),(h) 15–20, (d),(i) 20–25, and (e),(j) 25–30 μm. Arrows and rectangles are described in the text, and Arabic and capital Greek numbers are used for rectangles and arrows, respectively.

found that hexagonal cell structures (i.e., open cell structures) are produced in the pristine experiment. Precipitation occurs in the pristine experiment at the center of the hexagonal cells. This cloud structure and its aerosol dependence are the same as found by Wang and Feingold (2009), and are also consistent with proposals of cloud field changes caused by aerosol effects (Twomey 1974; Albrecht 1989).

Figure 4 shows CFODDs obtained from model results at $t = 6$ h, while Fig. 5 presents CFODDs obtained from satellite observations in the East Asian region (Figs. 5a–e) and in the California coast region (Figs. 5f–j).

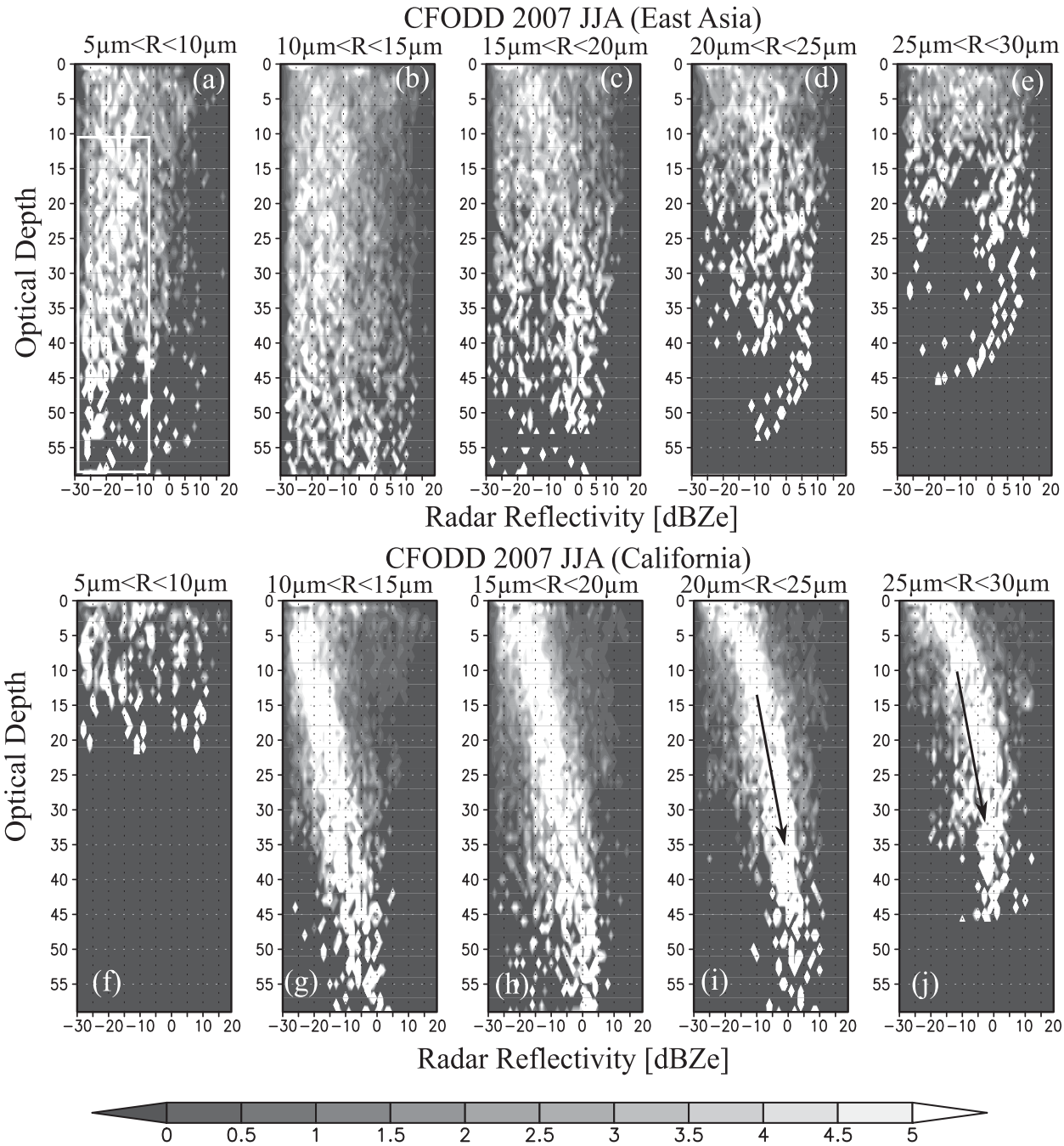

FIG. 5. CFODDs obtained from satellite observations in (a)–(e) East Asia (20°–40°N, 120°–140°E) and (f)–(j) California (20°–40°N, 115°–135°W), divided by RE = (a),(f) 5–10, (b),(g) 10–15, (c),(h) 15–20, (d),(i) 20–25, and (e),(j) 25–30 μm. Arrows and rectangles are described in the text.

The CFODDs shown in Figs. 4a–e are obtained from the polluted experiment and indicate that there are relatively few large particles (i.e., RE $>$ 20 μm) and none with RE $>$ 25 μm. In the upper part of cloud cells, the radar reflectivity of fine particles (i.e., RE $<$ 10 μm) decreases as the COD decreases from 3 to 0, as indicated by arrow V in Fig. 4a, after displaying an increasing tendency in the deeper part of the cloud layer, as shown by arrow II in Fig. 4a. These patterns were also found in satellite observations by S10 in their CFODDs, as shown by arrows ii and v in Fig. 1. S10 interpreted these patterns as showing that the decrease of radar reflectivity

toward the cloud top [i.e., arrow v in Fig. 1] corresponds to the evaporation of cloud particles invoked by cloud-top entrainment, and the increase in reflectivity (i.e., arrow ii in Fig. 1) corresponds to the condensation growth of uplifted cloud particles. Based on the insistence of S10, we called these patterns the "cloud-top entrainment pattern" (CTE pattern) and the "condensation pattern", respectively. The radar reflectivity of small particles (i.e., RE < 15 μm) is almost constant in the COD range 10–60, as indicated by arrow I in Fig. 4a, which was also found by S10 using satellite observations [shown by arrow i in Fig. 1]. We think that this pattern corresponds to the movement of cloud particles from cloud bottom to cloud top by updraft, and henceforth we call this an "updraft pattern."

Figures 4f–j show CFODDs obtained in the pristine experiment. In this case, small particles (i.e., RE $<$ 15 μm) do not exist in the optically deep region, whereas the radar reflectivity of large particles (i.e., RE > 20 μm) increases with the COD, as shown by arrow III in Figs. 4i and 4j. N10 and S10 interpreted this pattern as showing that cloud particles grow by collision/coagulation processes and then fall under gravity to the lower part of the CFODD. Henceforth, we refer to this as a "collision pattern." This pattern is not clear in Figs. 4d and 4e for the polluted case. Figures 4f–j show that patterns II and V in Fig. 4b are also produced in Fig. 4g, but pattern I (i.e., the updraft pattern) is not produced in the polluted case.

Figures 5a–e show CFODDs obtained from satellite observations in East Asia, where the amount of aerosol is significantly larger than the global average (Nakajima et al. 2001; Remer et al. 2005; Matsui et al. 2006). These correspond to the polluted condition in this study. In Fig. 5a, a constant radar reflectivity area (i.e., the updraft pattern) is produced, with a slightly increasing reflectivity with decreasing COD. This behavior was also simulated by the model (Fig. 4a).

Figures 5f–j are CFODDs obtained from satellite observations off the coast of California, where the amount of aerosol is small, corresponding to the pristine condition in this study. In this case, the collision pattern is clear, whereas the updraft pattern cannot easily be discerned. This structure was also reproduced by the model-derived CFODDs in the pristine experiment (Figs. 4f–j).

b. Growth stage of clouds represented in CFODDs

In the previous section, we confirmed that CFODDs simulated by the present model reproduce the characteristics of satellite-derived CFODDs. This confirmation justifies a more detailed use of the present model to identify the main growth processes that characterize the CFODD, which is one of the objectives of this study. For this purpose, we applied a cloud microphysics zero-dimensional box model to the simulated cloud field to identify the dominant processes that characterize each of the cloud state points composing the CFODD. This box model is a standalone version of the microphysical module of the UT-ACBM. It calculates the time evolution of SDFs using only the cloud microphysical processes, and assumes that the cloud dynamical state (i.e., temperature, pressure, and supersaturation) is given and fixed. In the present calculation, the initial value of temperature and pressure are set to 284 K and 800 hPa, respectively, which correspond to the mean atmospheric conditions of the cloud layer calculated by the present 3D model. To check the difference between the growth of SDF in a saturated air mass and that in an unsaturated air mass, we set two types of initial values of supersaturation: 0.5% and -0.01%. The box model calculates the condensation (evaporation) process when the value of supersaturation is positive (negative). Initial SDFs are given by the averaged SDF from the 3D model. Box model calculations are performed for 10 min with a time step $dt = 0.5$ s. For a sensitivity experiment, the box model calculations are also performed without either the condensation or collision processes.

As discussed in the previous section and S10, arrows II and V appearing in rectangle 1 of Fig. 4a correspond to the evaporation process at the cloud top and condensation growth in the cloud layer. Arrow III in rectangle 2 shows the conversion from cloud to rain by the collision/coagulation process. However, we need a validation of this interpretation. To verify the interpretation, we investigate the SDFs of the clouds in rectangles 1 and 2 of Figs. 4a and 4i, respectively. Figure 6 shows the averaged SDFs of rectangles 1 and 2, and the SDFs obtained by the box model calculations at $t = 10$ min from the start of box model calculations. It can be seen in this figure that the SDF of clouds in rectangle 1 is a monomodal shape. The peak value of the mode at around 20 μm grows (shrink) with time when all growth processes are active in saturated (unsaturated) air mass, as shown by the dotted curve. However, the peak value does not increase (decrease) without the condensation (evaporation) process in a saturated (unsaturated) air mass, as shown by the dashed curve, whereas it does increase (decrease) without the collision process in a saturated (unsaturated) air mass, as indicated by the dot-dashed curve. This means that cloud particles located in rectangle 1 of the CFODD grow mainly by condensation with saturated air mass, and they shrink through the evaporation process with an unsaturated air mass; the arrows in rectangle 1 of Fig. 4a show the active condensation or evaporation processes, respectively.

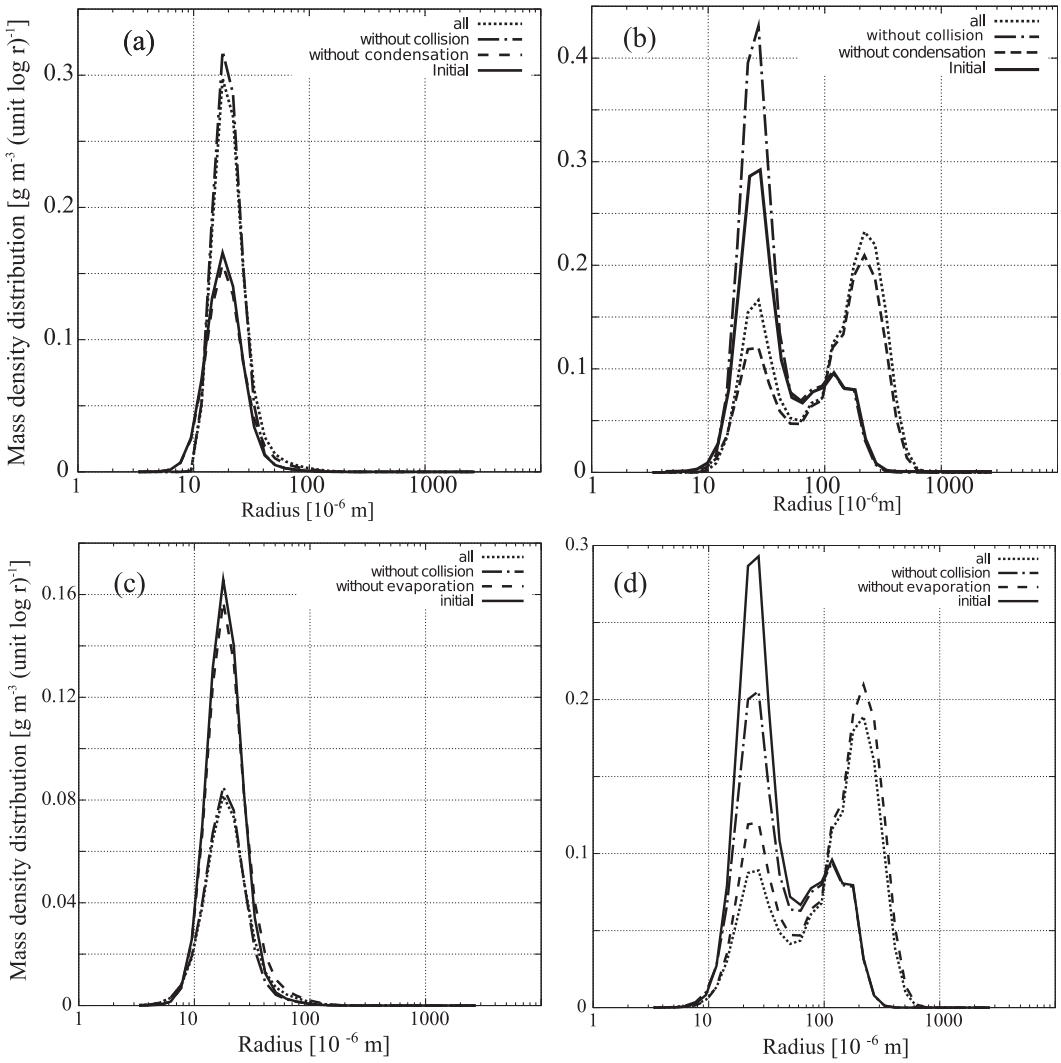

FIG. 6. Mass density size distribution functions (SDFs) averaged over (a),(c) rectangle 1 in Fig. 4a and (b),(d) rectangle 2 in Fig. 4i, and SDFs calculated by a box model after 10 min with (a),(b) saturated and (c),(d) unsaturated air mass. Solid lines indicate the initial SDFs for the box model calculation. Dotted, dashed, and dot-dashed lines show SDFs obtained at 10 min after the start of calculation by the box model with condensation/evaporation and collision processes, without condensation/evaporation process, and without collision processes, respectively.

The SDF in rectangle 2 of Fig. 4i is of bimodal shape. The peak of the large mode grows from 100 to about 130 μm because of the conversion of water from cloud/drizzle particles to rain, as calculated by the box model with all processes included (shown by the dotted curve), regardless of the value of supersaturation. In contrast, the large mode does not grow without the collision process, as shown by the dot-dashed curve in Figs. 6b and 6d. This result means that cloud particles located in rectangle 2 grow mainly by the collision process, regardless of the value of supersaturation; the arrow in rectangle 2 represents conversion from cloud to drizzle or rain by the collision process.

c. *The detailed discussion*

In the previous section, we confirmed growth stage shown in the modes on CFODDs by using a box model. The box model calculations show that the condensation pattern, CTE pattern, and collision pattern correspond to condensation, evaporation at cloud top, and the collision process of cloud growth. Although we achieve one of the objectives (i.e., confirmation of interpretation about cloud growth stage) through the analyses in the previous section, it is interesting to discuss the effects of drizzle on CFODDs because many previous studies discussed effects of drizzle on warm clouds. In addition,

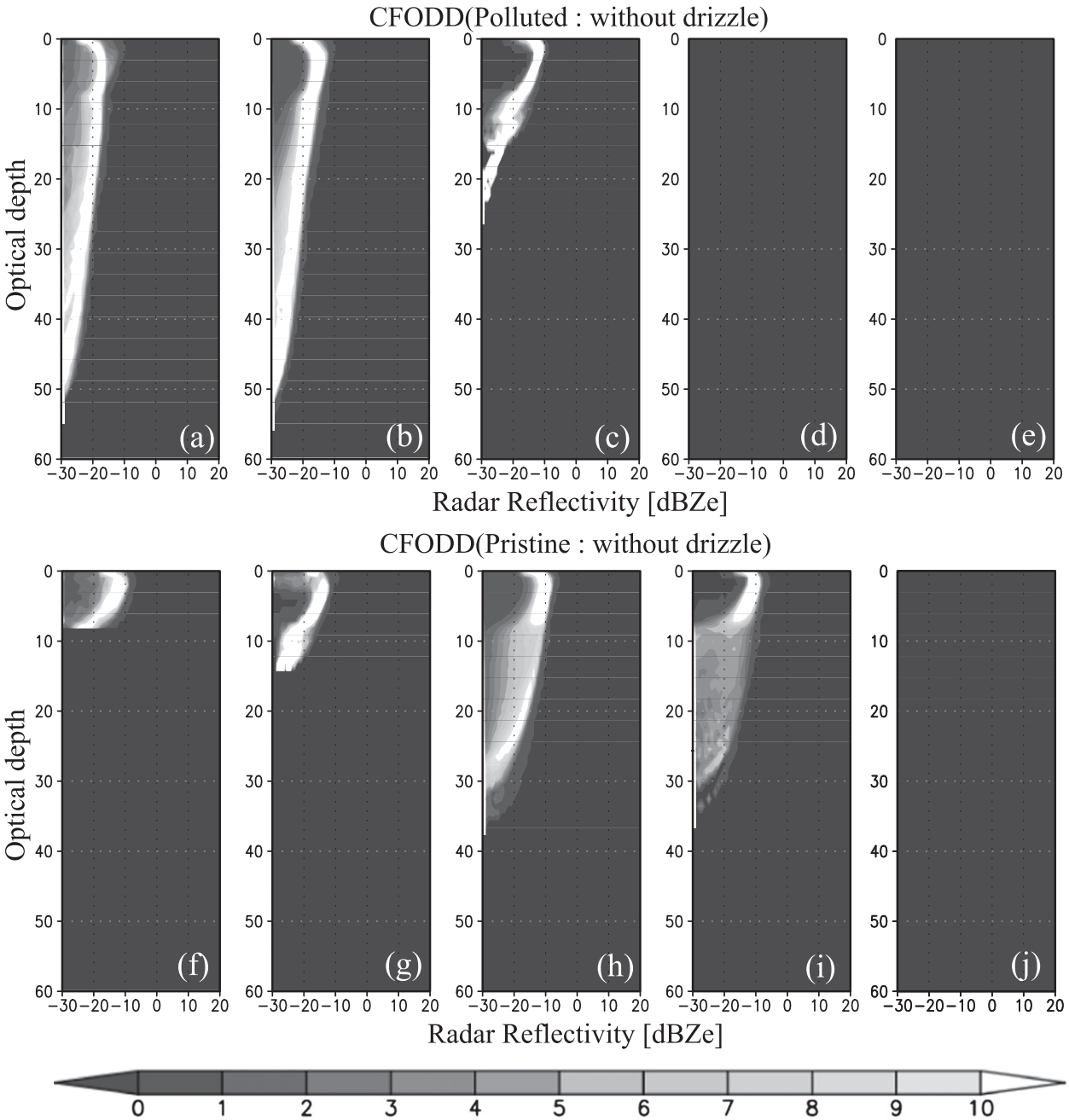

FIG. 7. As in Fig. 4, but calculated without drizzle particles, whose effective radii are over 30 μm.

a question is generated: why are the updraft patterns only shown in the CFODD of the polluted experiment, although the transportation of cloud particles by updrafts can occur in both the pristine and the polluted experiments? These discussions will be conducted in this section.

We first discuss effects of drizzle (defined in this study as cloud particles with radii larger than 30 μm) on CFODDs through comparisons of CFODDs obtained from the results of radar simulator calculation without drizzle particles with CFODDs obtained from the results with all cloud particles including drizzle particles. The CFODDs without drizzle particles are shown in Fig. 7. It is seen that collision patterns disappear from the CFODD without drizzle and the other patterns exist without drizzle. This result shows that the collision pattern mainly consists of drizzle particles, and a collision pattern is one of the signs indicating the existence of drizzle particles.

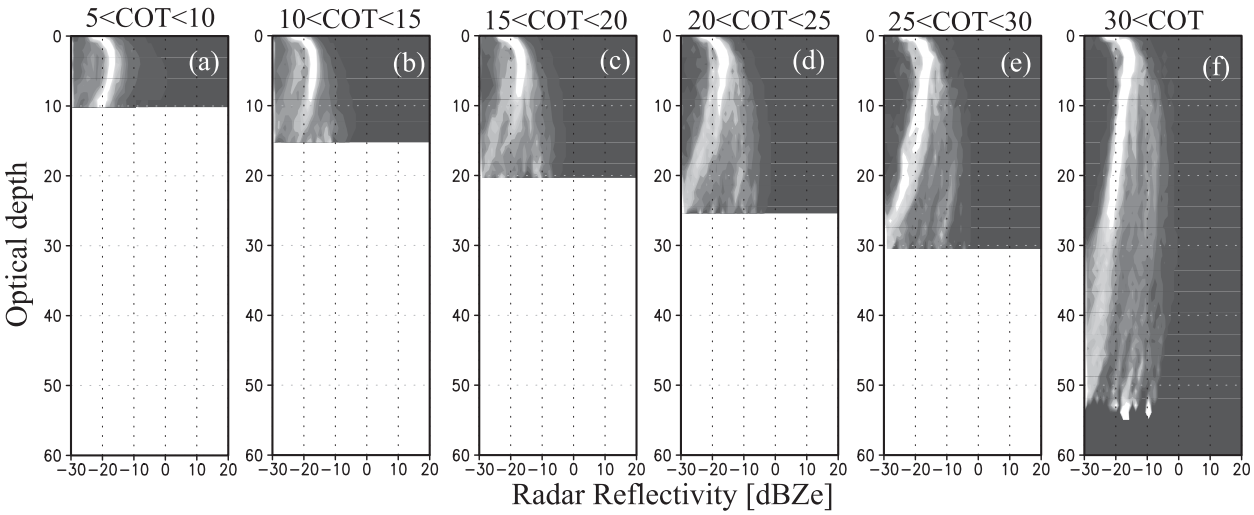

FIG. 8. CFODD obtained from the clouds, whose COT is (a) from 5 to 10, (b) from 10 to 15, (c) from 15 to 20, (d) from 20 to 25, (e) from 25 to 30, and (f) over 30, simulated by the polluted experiment.

Second, we discuss the question: why are the updraft patterns only shown in the CFODD obtained from the polluted experiment? To answer this question, we must consider both the condensation pattern and the updraft pattern because it can be inferred that the condensation process can occur during transportation of cloud particles by an updraft. The inference gives us an idea that the condensation pattern can be included in the updraft pattern. To clarify this, CFODDs divided by COT (total COD) are useful. Figure 8 shows CFODDs, where the range of effective radius is 5–10 μm, obtained from the clouds of polluted experiment, which are categorized by the range of COT. It is found that radar reflectivity increases monotonically with decreasing COD (i.e., condensation pattern) regardless of the COT range. The condensation pattern of optically thin clouds starts from optically thin area, while the pattern of optically thick clouds starts from an optically thick area and moves to an optically thin area. The result shows that the updraft pattern consists of condensation patterns of several clouds where COT varies, and the updraft pattern cannot be reproduced in the pristine experiment because optically thick clouds are rare in the pristine experiment. Based on this result, we can conclude that the updraft pattern should be also considered a type of condensation pattern, too.

d. *Time evolution of CFODDs*

The analyses in the preceding subsections were conducted using snapshot results at $t = 6$ h after the start of the calculation, and the satellite analyses by S10 were conducted using observational data accumulated over several months. For further verification of the interpretation of N10 and S10, therefore, an analysis of the time evolution of CFODDs is important. Although it is difficult to investigate the time evolution of CFODDs from satellite observation, because the A-Train constellation flies in a sun-synchronous polar orbit near 1330 local time, we can study the simulated time evolution of CFODDs.

Figure 9 shows CFODDs obtained from the pristine experiments at 2.5 and 6 h after the start of each calculation. We show only a CFODD of the pristine experiments, which reproduce the collision mode, because we want to compare time evolution of a model-derived CFODD with that based on the continuous ''collision'' equation shown later.

In the early stages of the calculation ($t = 2.5$ h), most contours are located in the optically thin area for COD < 22, and the amount of large particles (i.e., RE > 25 μm) is small. The COD gradually increases with time (not shown). In the later stages of the calculation ($t = 6$ h), the contours are widely spread from the optically thin area to the thick area, and large particles are generated. To compare the cloud growth in the CFODDs with the theoretical growth calculation, we introduce the continuous growth model (e.g., Rogers and Yau 1989), which describes how a collector drop with radius r grows by falling through and sweeping out the population of smaller cloud particles, whose mass concentration is denoted by q_c (g m^{-3}). The growth rate of a particle due to this collection process is expressed as (e.g., Rogers and Yau 1989)

$$\frac{dr}{dt} = \frac{E_c V(r)}{4\rho_w} q_c, \tag{14}$$

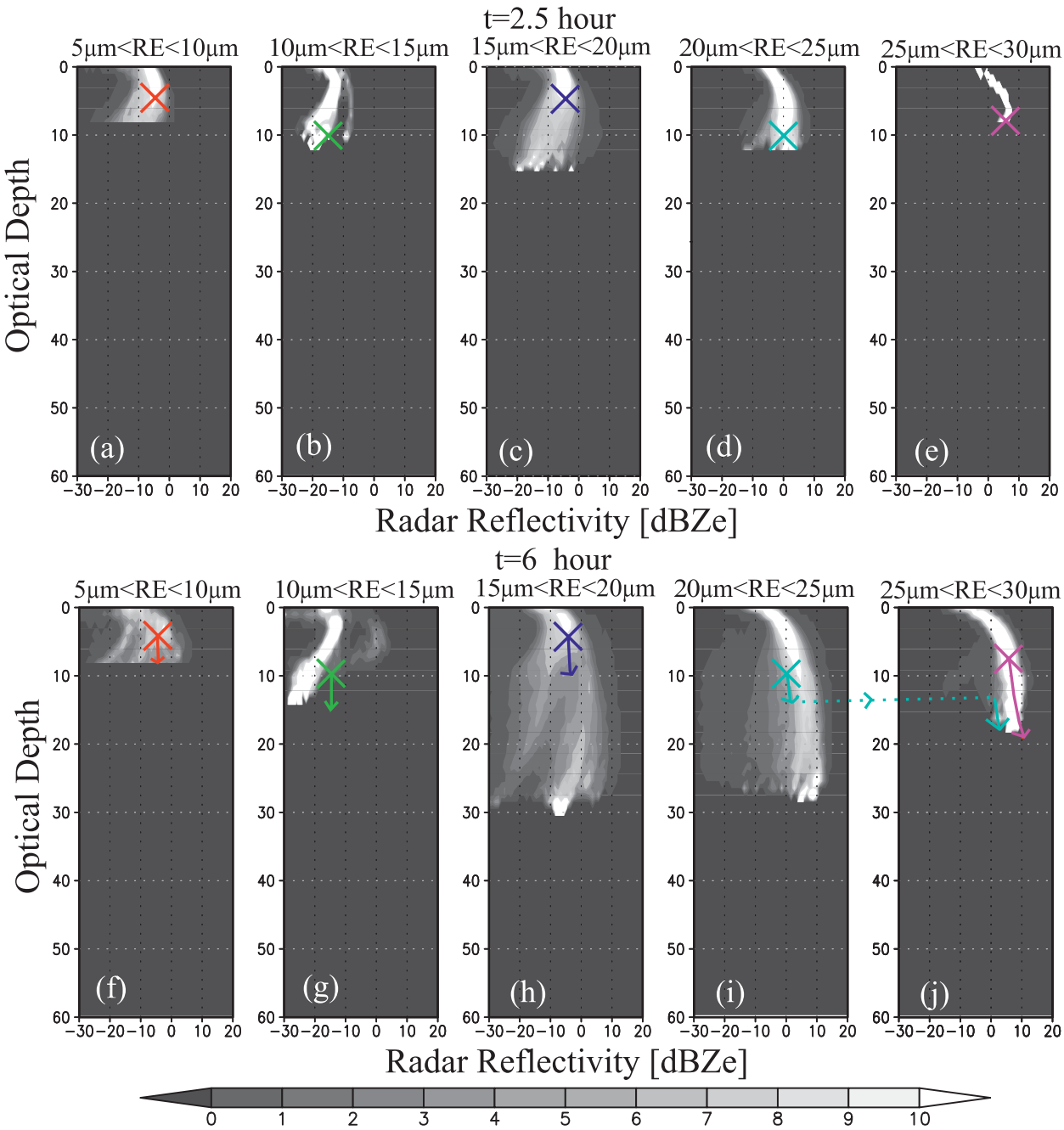

FIG. 9. As in Figs. 4f–j, but at t = (a)–(e) 2.5 h and (f)–(j) 6 h. Arrows are orbits on a CFODD during a 3.5-h calculation by a continuous growth model with starting point (cross) at (a) $\tau_d = 8$, $Z_e = -10$ (dBZ_e) (red), (b) $\tau_d = 10$, $Z_e = -5$ (dBZ_e) (green), (c) $\tau_d = 5$, $Z_e = -5$ (dBZ_e) (dark blue), (d) $\tau_d = 10$, $Z_e = 0$ (dBZ_e) (light blue), and (e) $\tau_d = 8$, $Z_e = 5$ (dBZ_e) (orange).

where $V(r)$ is the terminal velocity of the collector drop and E_c is the collision efficiency; E_c is obtained from a collection kernel (Long 1974), $V(r)$, and an assumption that the coalescence efficiency is 1. The upward air velocity is often neglected, as it is much smaller than the fall velocity (e.g., Rogers and Yau 1989), and so Eq. (14) leads to the growth rate with respect to height:

$$\frac{dr}{dh} = \frac{dr}{dt}\frac{dt}{dh} = -\frac{dr}{dt}\frac{1}{V(r)} = -\frac{E_c q_c}{4\rho_w}. \tag{15}$$

The negative sign means that r increases as the particle descends. Dividing Eq. (15) by r, we obtain

$$\frac{dr}{r} = -\frac{E_c}{4\rho_w}\frac{q_c dh}{r}. \tag{16}$$

If we relate the fractional change in r to that in Z_e as

$$\frac{dZ_e}{Z_e} = \alpha\frac{dr}{r} \quad \text{or} \quad d(\ln Z_e) = \alpha d(\ln r), \tag{17}$$

and the cloud water path to the optical depth change as

$$d\tau_d = -\frac{3}{2}\frac{1}{\rho_w}\frac{q_c dh}{r}, \tag{18}$$

then Eq. (16) leads to

$$\frac{dZ_e}{Z_e} = \frac{\alpha}{6}E_c d\tau_d, \tag{19}$$

where α differs according to the cloud stage depending on the dominant water conversion process. A typical value of $\alpha = 6$ is taken when the number concentration is conserved, whereas $\alpha = 3$ when the mass concentration is conserved. As these situations correspond to the condensational growth and coalescence processes, respectively (Suzuki and Stephens 2008), it may be natural to assume $\alpha \sim 3$ for the collection process examined here. To derive the time evolution of radar reflectivity, Eq. (14) can be reformulated as

$$\frac{dr}{d(\ln r)}\frac{d(\ln r)}{dt} = r\frac{d(\ln r)}{dt} = \frac{E_c V(r)}{4\rho_w}q_c, \tag{20}$$

so that Eqs. (17) and (20) lead to an equation for the time evolution of the radar reflectivity:

$$\frac{d(\ln Z_e)}{dt} = \frac{3E_c V(r)q_c}{4\rho_w r}, \tag{21}$$

and Eqs. (19) and (21) give an equation for the time evolution of the optical depth:

$$\frac{d\tau_d}{dt} = \frac{3V(r)q_c}{2\rho_w r}. \tag{22}$$

Solving Eqs. (14), (21), and (22), we can calculate the growth trajectory of a collector drop in the CFODD, assuming a typical value of $q_c = 0.2$ g m^{-3} in the pristine experiment. The arrows in Fig. 9 are examples of trajectories over a 3.5-h period from the states indicated by cross symbols at $t = 2.5$ h. The starting points shown as cross symbols in Fig. 9 are at the optically deepest points of contour value = 10% dBZ^{-1} in Figs. 9a–e, for which detailed values are shown in Table 1. These growth trajectories show how cloud droplets at each position on the CFODD move during the 3.5-h period. Trajectories of mid- and large-sized particles (i.e., RE = 15 and 20 μm at the start time of the continuous model) move along the ridge of the CFODD contours, indicating that water collection by the collision process is dominant, while the trajectories of coarse particles (i.e., RE = 25 μm at the model start time) deflect from the dense contour area of the CFODD, indicating that cloud particles grow into coarse droplets and are lost from the cloud layer as precipitation at a later time in the simulation. This interpretation is supported by the surface precipitation shown in Fig. 3 in the pristine experiment.

TABLE 1. Initial values of radar reflectivity, COD, and RE whose growth trajectories are shown in Fig. 9, calculated by the continuous collection model.

Category	Fig. 9a	Fig. 9b	Fig. 9c	Fig. 9d	Fig. 9e
Initial reflectivity (dBZ_e)	−5	−15	−5	0	5
Initial τ_d	8	10	5	10	8
Initial RE (μm)	5	10	15	20	25

Trajectories of fine particles (i.e., RE < 10 μm at the model start time) move along an isoline of radar reflectivity, indicating that the growth of these particles is not significant enough to increase the radar reflectivity by collision process. This fact demonstrates why the collection process is not dominant for these small particles, as discussed in section 3b. It is easily understood from Eqs. (21) and (22) that these trajectories are mainly generated by the strong size dependence of terminal velocity, as also shown in Fig. 10. This analysis proves that CFODDs can depict a cloud particle growth regime that drastically changes at a particle radius of around 20 μm between large and small particle regimes with and without significant particle growth by the collision/coagulation process. This critical particle radius is useful for classifying CFODDs.

4. Discussion

In the previous sections, the interpretation of the previous studies is verified through the analyses of the model results. Although the analyses are meaningful, there are several issues to discuss. The issues are 1) validity of vertical axis of CFODDs and 2) effects of vertical grid resolution of cloud model. These points are discussed in this section.

a. Benefit of taking COD as the vertical axis of CFODD

We first discuss the vertical axis of CFODD, COD, since transferring from geometrical depth of clouds to

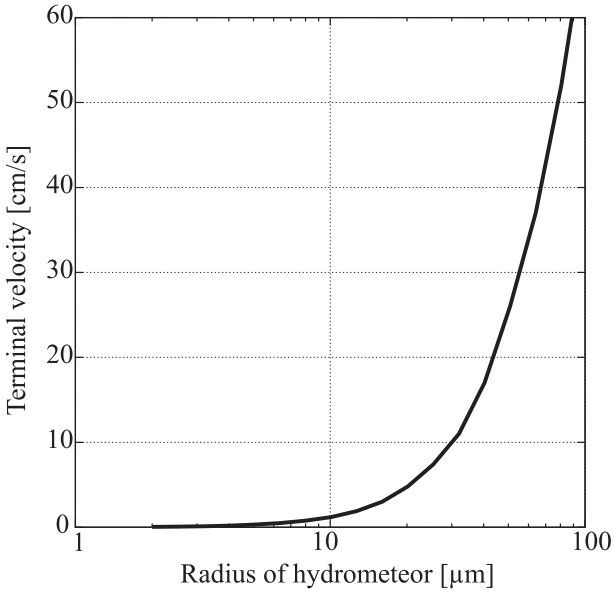

FIG. 10. Terminal velocity of cloud particles.

COD can cause errors. To show the benefit of taking COD as the vertical axis, a contoured frequency diagram between cloud geometrical depth (hereafter CFGDD), instead of COD, and radar reflectivity is created. The CFGDD obtained from the pristine experiment is shown in Fig. 11. It is seen that the condensation pattern, collision pattern, and CTE pattern are also reproduced in CFGDD, but the condensation pattern and collision pattern are separated into two parts (see Figs. 11b,d). The first part is located in a geometrically deep area and the second in a geometrically thinner area. The two parts originate from geometrically thick and thin clouds, respectively (not shown). The separation of the modes is not shown in CFODD because CFODD takes COD as its vertical axis. This is the one of the benefits to taking COD as the vertical axis of CFODD when discussing the growth process of clouds.

We must refer to an important point from this analysis (although the vertical axis of CFODD has advantages), namely the relationship between the geometrical thickness of the clouds simulated by the model and the sampling volume of *CloudSat* CPR. It is seen from Fig. 11 that the cloud geometrical thickness simulated by the model is from 400 to 800 m. This geometrical thickness corresponds to one or two sampling volumes of *CloudSat* CPR, and CFODD obtained from satellite observation does not always show the characteristics of warm clouds simulated in this study. This is the one of the drawbacks of this study. We must conduct global simulations of cloud-resolving models to discuss the characteristics of CFODD in more detail. In addition, vertical resolution of the model is much finer than the sampling volume. We will discuss the effects of vertical resolution in next section.

b. *Effects of the vertical resolution of the model*

We next discuss the effects of vertical grid resolution since the vertical resolution of the model (dz = 10 m for

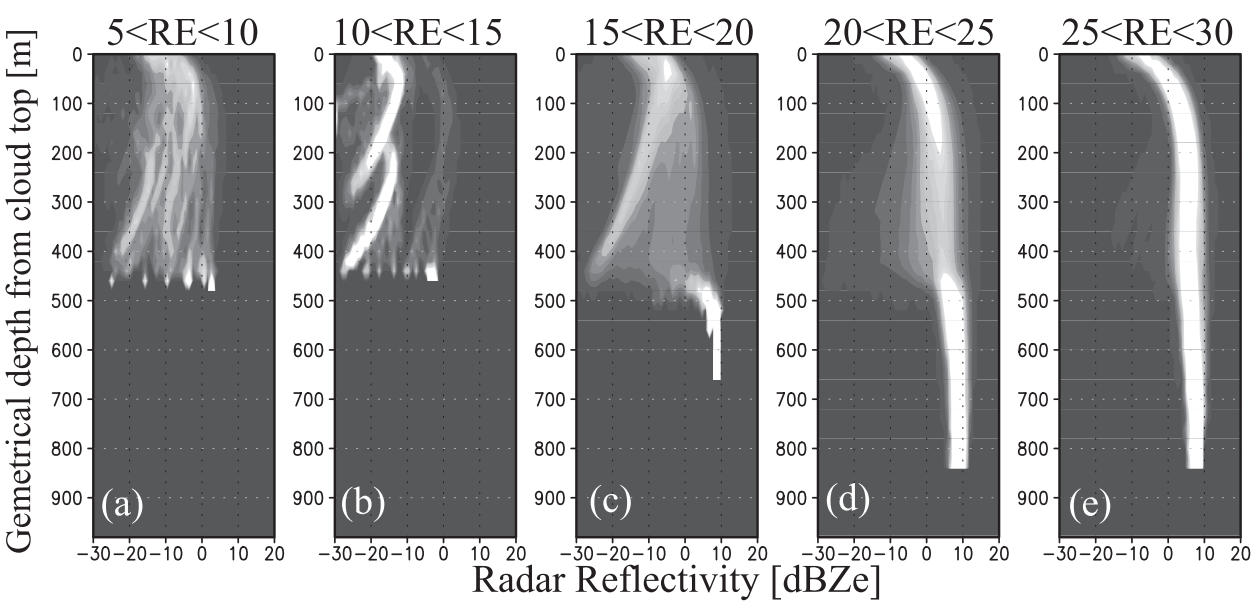

FIG. 11. Contoured frequency diagram of cloud geometrical depth (CFGDD) at t = 6 h obtained from the pristine experiments, divided by RE = (a) 5–10, (b) 10–15, (c) 15–20, (d) 20–25, and (e) 25–30 μm.

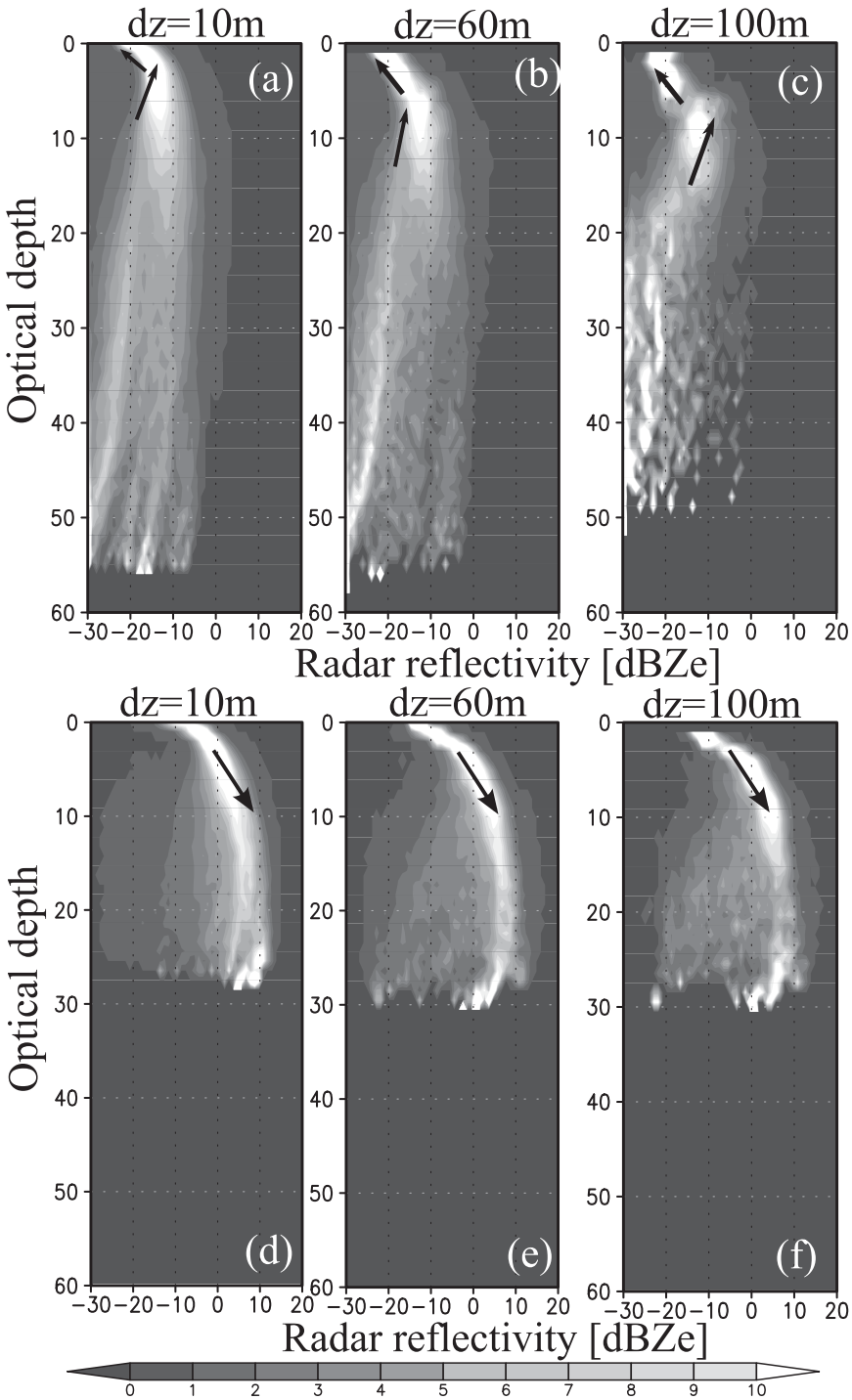

FIG. 12. CFODDs at t = 6 h obtained from (a)–(c) polluted experiments, whose RE = 5–10 μm, and (d)–(f) pristine experiments, whose RE = 20–25 μm, calculated by dz = (a),(d) 10-, (b),(e) 60-, and (c),(f) 100-m horizontal grid spacing. Arrows and rectangles are described in the text.

calculation of radiative transfer) is much higher than sampling volume of CPR (dz = 480 m).

To investigate the effects of vertical grid resolution, we perform calculations of the radar simulator changing vertical grid resolution and create CFODDs by using radar reflectivity calculated by each grid resolution. The vertical grid resolutions of the calculation are 10, 60, and 100 m. The CFODDs calculated by this sensitivity calculation are shown in Fig. 12. It is seen from Fig. 12 that the condensation pattern and CTE pattern are separated in the CFODDs calculated by coarse vertical grid resolution (i.e., dz = 100 m). The difference results from the depth of each grid of volumes. Coarse grid spacing makes the difference of COD between each grid and its neighbor grid large, which can separate the modes in CFODD. This characteristic is also seen in CFODDs of satellite observation (Fig. 1a), whose vertical grid resolution is coarse (i.e., 480 m).

Although vertical grid resolution has some effect on CFODDs, the condensation, CTE, and collision pattern are reproduced by the model regardless of the vertical grid resolution. From these results we can conclude that CFODDs obtained from the model simulations at much finer grid spacing than satellite observation are useful to interpret the cloud growth process.

5. Concluding remarks

In this paper, we calculated CFODDs from the results of a cloud ensemble simulation by a 3D numerical model, which assumed a dynamical condition off the California coast in the summer season. The simulated CFODDs reproduced the characteristic patterns obtained by satellite observations. The results and additional diagnostic tests by a box microphysics model showed that the clouds in rectangle 1 of Fig. 4a mainly grew by the condensation/evaporation process, while the clouds in rectangle 2 grew as a result of the collision/coagulation process. This result mostly supports the interpretations of previous studies about the dominant growth processes in warm cloud cells (N10; S10). Simulated CFODDs revealed that ''updraft'' and ''condensation'' patterns in CFODDs were mainly found in clouds in a polluted condition, whereas the ''collision'' pattern was mainly found in clouds in a pristine condition. Another analysis shows that updraft pattern does not always consist of updraft processes but rather consists of condensation patterns of several clouds, with different COTs.

The time evolutions of CFODDs are first calculated by using the results obtained from the model.

There are some differences between the CFODDs in this study and those of N10 and S10 (see our Fig. 1). There are dense contours in an optically deep area in the CFODDs of N10 and S10, and these differences result from the deficit of the experimental setup. We must conduct global-scale experiments in the future.

Acknowledgments. This study was supported by the Initiative on Promotion of Supercomputing for Young Researchers, from the Supercomputing division, Information Technology Center, University of Tokyo. Some authors were supported by Grant-in-Aid for JSPS Fellows 22-7893; some were supported by projects of JAXA/EarthCARE, JAXA/GCOM-C, MEXT/VL for Climate System Diagnostics, MOE/Global Environment Research Fund A-1101, NIES/GOSAT, and MEXT/RECCA/SALSA. Y. Sato was supported by the JSPS Institutional Program for Young Researcher Overseas Visits and greatly acknowledges Dr. Jorgen Jensen and Dr. Christpher S. Bretherton for their helpful advice. Some of the computations for this study were carried out using the Hitachi SR16000 of the computer facilities of the Research Institute of Information Technology, Kyushu University, and Hitachi SR11000, HA8000 of the Supercomputing division, Information Technology Center, University of Tokyo.

REFERENCES

Ackermann, A. S., and Coauthors, 2009: Large-eddy simulations of a drizzling, stratocumulus-topped marine boundary layer. *Mon. Wea. Rev.,* **137,** 1083–1110.

Albrecht, B. A., 1989: Aerosols, cloud microphysics, and fractional cloudiness. *Science,* **245,** 1227–1230.

——, D. A. Randall, and S. Nicholls, 1988: Observations of marine stratocumulus clouds during FIRE. *Bull. Amer. Meteor. Soc.,* **69,** 618–626.

Barkstrom, B. R., 1984: The Earth Radiation Budget Experiment (ERBE). *Bull. Amer. Meteor. Soc.,* **65,** 1170–1186.

——, and G. L. Smith, 1986: The Earth Radiation Experiment: Science and implementation. *Rev. Geophys.,* **24,** 379–390.

Brenguier, J.-L., H. Pawlowska, L. Schüller, R. Preusker, J. Fischer, and Y. Fouquart, 2000: Radiative properties of boundary layer clouds: Droplet effective radius versus number concentration. *J. Atmos. Sci.,* **57,** 803–821.

Choi, I.-J., T. Iguchi, S.-W. Kim, S.-C. Yoon, and T. Nakajima, 2010: Simulation of aerosol effect on the microphysical properties of shallow stratocumulus cloud over East Asia region using a bin-based cloud resolving model. *Atmos. Chem. Phys. Discuss.,* **10,** 23 449–23 495.

Deardorff, J. W., 1980: Stratocumulus-capped mixed layers derived from a three-dimensional model. *Bound.-Layer Meteor.,* **18,** 495–527.

Feingold, G., S. M. Kreidenweis, B. Stevens, and W. R. Cotton, 1996: Numerical simulations of stratocumulus processing of cloud condensation nuclei through collision-coalescence. *J. Geophys. Res.,* **101** (D16), 21 391–21 402.

Han, Q., W. B. Rossow, and A. A. Lacis, 1994: Near-global survey of effective droplet radii in liquid water clouds using ISCCP data. *J. Climate,* **7,** 465–497.

Iguchi, T., T. Nakajima, A. P. Khain, K. Saito, T. Takemura, and K. Suzuki, 2008: Modeling the influence of aerosols on cloud microphysical properties in the East Asia region using a mesoscale model coupled with a bin-based cloud microphysics scheme. *J. Geophys. Res.,* **113,** D14215, doi:10.1029/2007JD009774.

Kawamoto, K., T. Nakajima, and T. Y. Nakajima, 2001: A global determination of cloud microphysics with AVHRR remote sensing. *J. Climate,* **14,** 2045–2068.

Khain, A. P., M. Ovtchinnikov, M. Pinsky, A. Pokrovsky, and H. Krugliak, 2000: Notes on the state-of-the-art numerical modeling of cloud microphysics. *Atmos. Res.,* **55,** 159–224.

Klein, S. A., and D. L. Hartmann, 1993: The seasonal cycle of low stratiform clouds. *J. Climate,* **6,** 1587–1606.

Long, A. B., 1974: Solutions to the droplet collection equation for polynomial kernels. *J. Atmos. Sci.,* **31,** 1040–1052.

Low, R. D. H., 1969: A generalized equation for the solution effect in droplet growth. *J. Atmos. Sci.,* **26,** 608–611.

Ma, C.-C., C. R. Mechoso, A. W. Robertson, and A. Arakawa, 1996: Peruvian stratus clouds and the tropical Pacific circulation: A coupled ocean–atmosphere GCM study. *J. Climate,* **9,** 1635–1645.

Mace, G. G., R. Marchand, Q. Zhang, and G. Stephens, 2007: Global hydrometeor occurrence as observed by CloudSat: Initial observations from summer 2006. *Geophys. Res. Lett.,* **34,** L09808, doi:10.1029/2006GL029017.

Matsui, T., H. Masunaga, S. M. Kreidenweis, R. A. Pielke Sr., W.-K. Tao, M. Chin, and Y. J. Kaufman, 2006: Satellite-based assessment of marine low cloud variability associated with aerosol, atmospheric stability, and the diurnal cycle. *J. Geophys. Res.,* **111,** D17204, doi:10.1029/2005JD006097.

Nakajima, T., and M. D. King, 1990: Determination of the optical thickness and effective particle radius of clouds from reflected solar radiation measurements. Part I: Theory. *J. Atmos. Sci.,* **47,** 1878–1893.

——, ——, J. D. Spinhirne, and L. F. Radke, 1991: Determination of the optical thickness and effective particle radius of clouds from reflected solar radiation measurements. Part II: Marine stratocumulus observations. *J. Atmos. Sci.,* **48,** 728–751.

——, M. Tsukamoto, Y. Tsushima, A. Numaguti, and T. Kimura, 2000: Modeling of the radiative process in an atmospheric general circulation model. *Appl. Opt.,* **39,** 4869–4878.

——, A. Higurashi, K. Kawamoto, and J. E. Penner, 2001: A possible correlation between satellite-derived cloud and aerosol microphysical parameters. *Geophys. Res. Lett.,* **28,** 1171–1174.

Nakajima, T. Y., and T. Nakajima, 1995: Wide-area determination of cloud microphysical properties from NOAA AVHRR measurements for FIRE and ASTEX regions. *J. Atmos. Sci.,* **52,** 4043–4059.

——, K. Suzuki, and G. L. Stephens, 2010a: Droplet growth in warm water clouds observed by the A-Train. Part I: Sensitivity analysis of the MODIS-derived cloud droplet sizes. *J. Atmos. Sci.,* **67,** 1884–1896.

——, ——, and ——, 2010b: Droplet growth in warm water clouds observed by the A-Train. Part II: A multisensory view. *J. Atmos. Sci.,* **67,** 1897–1907.

Okamoto, H., S. Iwasaki, M. Yasui, H. Horie, H. Kuroiwa, and H. Kumagai, 2003: An algorithm for retrieval of cloud microphysics using 95-GHz cloud radar and lidar. *J. Geophys. Res.,* **108,** 4226, doi:10.1029/2001JD001225.

——, and Coauthors, 2007: Vertical cloud structure observed from shipborne radar and lidar: Midlatitude case study during the MR01/K02 cruise of the research vessel Mirai. *J. Geophys. Res.,* **112,** D08216, doi:10.1029/2006JD007628.

——, and Coauthors, 2008: Vertical cloud properties in the tropical western Pacific Ocean: Validation of the CCSR/NIES/FRCGC GCM by shipborne radar and lidar. *J. Geophys. Res.,* **113,** D24213, doi:10.1029/2008JD009812.

Platnick, S., 2000: Vertical photon transport in cloud remote sensing problems. *J. Geophys. Res.,* **105,** 22 919–22 935.

——, M. D. King, S. A. Ackerman, W. P. Menzel, B. A. Baum, J. C. Riedi, and R. A. Frey, 2003: The MODIS cloud products: Algorithms and examples from *Terra*. *IEEE Trans. Geosci. Remote Sens.,* **41,** 459–473.

Pruppacher, H., and J. D. Klett, 1997: *Microphysics of Clouds and Precipitation*. 2nd ed. Springer, 954 pp.

Randall, D. A., J. A. Coakley Jr., C. W. Fairall, R. A. Kropfli, and D. H. Lenschow, 1984: Outlook for research on subtropical marine stratiform clouds. *Bull. Amer. Meteor. Soc.,* **65,** 1290–1301.

Remer, L. A., and Coauthors, 2005: The MODIS aerosol algorithm, products and validation. *J. Atmos. Sci.,* **62,** 947–973.

Rogers, R. R., and M. K. Yau, 1989: *A Short Course in Cloud Physics*. 3rd ed. Pergamon Press, 293 pp.

Rosenfeld, D., 2000: Suppression of rain and snow by urban and industrial air pollution. *Science,* **287,** 1793–1796.

Saito, K., and Coauthors, 2006: The operational JMA nonhydrostatic mesoscale model. *Mon. Wea. Rev.,* **134,** 1266–1298.

Sato, Y., T. Nakajima, K. Suzuki, and T. Iguchi, 2009: Application of a Monte Carlo integration method to collision and coagulation growth processes of hydrometeors in a bin-type model. *J. Geophys. Res.,* **114,** D09215, doi:10.1029/2008JD011247.

Savic-Jovcic, V., and B. Stevens, 2008: The structure and mesoscale organization of precipitating stratocumulus. *J. Atmos. Sci.,* **65,** 1587–1605.

Sekiguchi, M., and T. Nakajima, 2008: A *k*-distribution-based radiation code and its computational optimization for an atmospheric general circulation model. *J. Quant. Spectrosc. Radiat. Transf.,* **109,** 2779–2793.

Stephens, G. L., and Coauthors, 2002: The CloudSat mission and the A-Train. *Bull. Amer. Meteor. Soc.,* **83,** 1771–1790.

——, and Coauthors, 2008: The CloudSat mission: Performance and early science after the first year of operation. *J. Geophys. Res.,* **113,** D00A18, doi:10.1029/2008JD009982.

Stevens, B., and Coauthors, 2005: Evaluation of large-eddy simulations via observations of nocturnal marine stratocumulus. *Mon. Wea. Rev.,* **133,** 1443–1462.

Suzuki, K., and G. L. Stephens, 2008: Global identification of warm cloud microphysical processes with combined use of A-Train observations. *Geophys. Res. Lett.,* **35,** L08805, doi:10.1029/2008GL033590.

——, T. Nakajima, T. Y. Nakajima, and A. Khain, 2006: Correlation pattern between effective radius and optical thickness of water clouds simulated by a spectral bin microphysics cloud model. *SOLA,* **2,** 116–119, doi:10.2151/sola.2006-030.

——, T. Y. Nakajima, and G. L. Stephens, 2010: Particle growth and drop collection efficiency of warm clouds as inferred from joint CloudSat and MODIS observations. *J. Atmos. Sci.,* **67,** 3019–3032.

Takemura, T., T. Nozawa, S. Emori, T. Y. Nakajima, and T. Nakajima, 2005: Simulation of climate response to aerosol direct and indirect effects with aerosol transport-radiation model. *J. Geophys. Res.,* **110,** D02202, doi:10.1029/2004JD005029.

Twomey, S., 1974: Pollution and the planetary albedo. *Atmos. Environ.,* **8,** 1251–1256.

vanZanten, M. C., and B. Stevens, 2005: Observation of the structure of heavily precipitating marine stratocumulus. *J. Atmos. Sci.,* **62,** 4327–4342.

Wang, H., and G. Feingold, 2009: Modeling mesoscale cellular structures and drizzle in marine stratocumulus. Part I: Impact of drizzle on the formation and evolution of open cells. *J. Atmos. Sci.,* **66,** 3237–3256.

Winker, D. M., J. Pelon, and M. P. McCormick, 2003: The CALIPSO mission: Spaceborne lidar for observation of aerosols and clouds. *Lidar Remote Sensing for Industry and Environment Monitoring III,* U. N. Singh, T. Itabe, and Z. Liu, Eds., International Society for Optical Engineering (SPIE Proceedings, Vol. 4893), doi:10.1117/12.466539.

——, W. H. Hunt, and M. J. McGill, 2007: Initial performance assessment of CALIOP. *Geophys. Res. Lett.,* **34,** L19803, doi:10.1029/2007GL030135.